In Situ 3D Neutron Depolarization Study of the Transformation Kinetics and Grain Size Evolution During Cyclic Partial Austenite-Ferrite Phase Transformations in Fe-C-Mn Steels

Fang, H.; van der Zwaag, S.; van Dijk, N. H.

DOI
10.1007/s11661-018-4905-8

Publication date
2018

Document Version
Final published version

Published in
Metallurgical and Materials Transactions A: Physical Metallurgy and Materials Science

In Situ 3D Neutron Depolarization Study of the Transformation Kinetics and Grain Size Evolution During Cyclic Partial Austenite-Ferrite Phase Transformations in Fe-C-Mn Steels

H. FANG, S. VAN DER ZWAAG, and N.H. VAN DIJK

We have analyzed the evolution of the ferrite fraction and average ferrite grain size during partial cyclic austenite-to-ferrite and ferrite-to-austenite phase transformations in an Fe-0.25C-2.1Mn (wt pct) steel using three-dimensional neutron depolarization (3DND). In the 3DND experiments, the ferrite fraction is derived from the rotation angle of the neutron polarization vector, and the average grain size is determined from the shortening of the polarization vector. From these, the number density of ferrite grains is derived, which indicates that grain nucleation is negligible during partial cycling in the intercritical regime and that all transformation kinetics can be attributed to growth processes only. In the multiple successive cyclic partial transformations, the interfacial migration rate was found to be sluggish due to Mn partitioning. The transformation kinetics determined with 3DND was compared to the predicted behaviors for diffusion-controlled simulations under local equilibrium and para-equilibrium interfacial conditions. It was found that the simulation predictions under local equilibrium only qualitatively capture the transformation kinetic with a difference of one order of magnitude in the variation in the ferrite fraction during cycling. The cyclic behavior of this Fe-0.25C-2.1Mn (wt pct) steel shows that the austenite-ferrite interface indeed migrates back and forth during cycling, while at the same time, there is a gradual increase in both the ferrite fraction and the average ferrite grain size over subsequent cycles. The intrinsic cyclic behavior is only visible after subtracting the effect of the progressive interfacial migration into austenite. The present study demonstrates the advantage of 3DND in studying partial cyclic phase transformations over conventional experimental approaches.

https://doi.org/10.1007/s11661-018-4905-8

I. INTRODUCTION

THE kinetics of the austenite-to-ferrite (γ-α) and the ferrite-to-austenite (α-γ) transformations in low-alloyed steels have attracted extensive attention due to their practical importance and scientific challenges.[1–5] During the austenite-to-ferrite transformation, the ferrite first nucleates at the preferred nucleation sites and subsequently grows into the austenite grains. As observed with synchrotron X-ray diffraction, ferrite nucleation occurs in a certain temperature (or time) range, where new nuclei continuously form until a maximum density is reached.[6] Once nucleated, the growth of a ferritic grain, *i.e.,* the interfacial migration, is controlled by interfacial mobility and diffusion of solute elements in the vicinity of the moving interface. To explore the effect of the alloying elements M (= Mn, Ni, Co, *etc.*) on interfacial migration in Fe-C-M steels, extensive studies have been performed using conventional isothermal or continuous heating and cooling experiments.[7–10] However, in such experiments where nucleation and interfacial migration take place simultaneously, the impossibility to determine the nucleation rate during the entire transformation process unavoidably leads to nonnegligible uncertainties in the derivation of the interfacial mobility and investigating the effect of the alloying elements. To avoid the effect of nucleation on the transformation kinetics, the concept

H. FANG is with the Fundamental Aspects of Materials and Energy Group, Faculty of Applied Sciences, Delft University of Technology, Mekelweg 15, 2629 JB Delft, The Netherlands and also with the Novel Aerospace Materials Group, Faculty of Aerospace Engineering, Delft University of Technology, Kluyverweg 1, 2629 HS Delft, The Netherlands. Contact e-mail: H.Fang@tudelft.nl S. VAN DER ZWAAG is with the Novel Aerospace Materials Group, Faculty of Aerospace Engineering, Delft University of Technology and also with the School of Materials Science and Engineering, Tsinghua University, Beijing 100084, China. N.H. VAN DIJK is with the Fundamental Aspects of Materials and Energy Group, Faculty of Applied Sciences, Delft University of Technology.
Manuscript submitted February 14, 2018.

Published online: 17 September 2018

of cyclic partial austenite-ferrite transformation, where the temperature is varied cyclically within the γ/α two-phase region, was recently proposed.[11] This cyclic approach has proven to be more informative in studying the effect of interfacial mobility and alloying elements on the rate of the interfacial migration as a result of the (assumed) absence of new nucleation events from the moment of the first inverse transformation cycle. This assumption is physically realistic and has been verified *ex-situ* by 2D metallographic cross sections.[12] A large number of dilatometric cyclic partial phase transformation measurements[11,12] and various modeling approaches such as DICTRA,[11] 1D mixed-mode modeling,[13] and 1D phase-field modeling[14,15] have been used to study the effect of alloying element M on the austenite decomposition rate and to obtain the interfacial mobility. These cyclic partial phase transformation studies reveal unexpected phenomena such as inverse and stagnant transformations as a result of various degrees of local partitioning of substitutional alloying elements at the moving austenite-ferrite interface. However, the key assumption behind the cyclic partial phase transformation approach that there are no, or only negligible, new nucleation events during cycling has not been verified by *in situ* experiments yet. To resolve this, we use three-dimensional neutron depolarization (3DND) to simultaneously measure the ferrite fraction and grain size during cyclic partial phase transformations in a low-alloyed construction steel. In the current study, the ferrite number density can be determined *in situ* during the cyclic partial phase transformation. The 3DND method also allows the *in situ* determination of the average grain size during the transformation, which can hardly be obtained from other physical *in situ* characterization techniques.

3DND is a powerful technique to characterize magnetic induction inside bulk materials at (sub)micron scale.[16,17] In a 3DND measurement, polarized neutrons demonstrate Larmor precession around a local magnetic field within a magnetized sample. After transmission through the sample, the mean magnetization causes a net rotation of the polarization vector, while a field variation due to magnetic inhomogeneities results in the decrease of the polarization vector. Therefore, the rotation angle measures the ferromagnetic phase fraction inside bulk materials. The shortening of the polarization vector determines the magnetic correlation length and thereby the mean size of the magnetic regions along the neutron path. A quantitative description of the relation between the correlation and the size of the magnetic particles in 3DND experiments was derived by Rosman and Rekveldt.[16] For the austenite-to-ferrite transformation in steels, the newly formed ferritic grains become magnetic below the Curie temperature (1043 K for pure iron), while the surrounding austenitic matrix remains paramagnetic and thereby effectively non-magnetic. This enables 3DND to determine the key microstructural features of the ferrite phase, *i.e.,* the ferrite volume fraction and the average ferrite grain size. Te Velthuis and coworkers[18] further developed the formulation of the 3DND method and applied it to study the austenite-to-ferrite transformation in medium carbon steels. In a recent study, we computationally analyzed the effect of the size distribution on the 3DND-derived microstructural parameters and found that the 3DND method, under certain conditions, may even yield information on the ferrite grain size distribution.[19] Therefore, the 3DND technique provides a powerful tool to simultaneously measure the ferrite fraction and the grain size within the bulk of steel samples. This technique has been used successfully to study austenite-to-ferrite[20] and austenite-to-pearlite[21] phase transformations in steels under isothermal conditions and during continuous cooling conditions.

In the current study, we carried out *in situ* 3DND measurements on cyclic partial phase transformations in an Fe-0.25C-2.1Mn (wt pct) steel. The ferrite fraction and the average grain size were derived explicitly as a function of time and temperature during cycling. The derived nuclei density and interfacial migration rate provide detailed information on the austenite-ferrite transformation behavior.

II. 3DND TECHNIQUE AND EXPERIMENTAL PROCEDURE

In a 3DND measurement, a 3 × 3 depolarization matrix $\hat{D}$ expresses the relationship between the polarization vector before ($\vec{P}^0$) and after ($\vec{P}'$) transmission through the sample by $\vec{P}' = \hat{D}\vec{P}^0$.[16,22] The components of the polarization vector are determined by the corresponding intensities detected by a ^{3}He detector parallel or antiparallel to the x, y, and z axis as expressed by

$$D_{ij} = \frac{I_s - I_{ij}}{I_s P_0}, \qquad [1]$$

where $i, j = x, y,$ or z represent the analyzed and initial polarization directions, respectively. P_0 is the degree of polarization of the incoming neutron beam and I_s is the shim intensity, which is given by $I_s = (I_{zz} + I_{zZ})/2$. The capital Z indicates a negative z direction. For the case with a net magnetization along the z axis, the neutron precession is around the plane perpendicular to the magnetization, resulting in a rotation angle of the polarization vector that can be expressed as

$$\varphi = \arctan\left(\frac{D_{xy} - D_{yx}}{D_{xx} + D_{yy}}\right). \qquad [2]$$

This rotation of the polarization vector is related to the mean magnetization of the sample[20,21]

$$\varphi = \eta\sqrt{c}L_x f\langle m_z\rangle \mu_0 M_s, \qquad [3]$$

where η is a geometric factor that accounts for the stray fields, $c = 2.15 \times 10^{29}\lambda^2\ \mathrm{T}^{-2}\ \mathrm{m}^{-4}$ is a constant with λ the neutron wavelength, L_x is the sample thickness, f is the volume fraction of the ferromagnetic phase, $\langle m_z\rangle$ is the average reduced magnetization in the direction of the applied magnetic field (z direction), μ_0 is the

permeability of vacuum, and M_s is the saturation magnetization of the ferromagnetic phase. In the current study, ferrite is the only ferromagnetic phase in the temperature range of interest. The $\langle m_z \rangle$ value was determined by fitting the magnetization hysteresis curves which were obtained by varying the applied magnetic field at a constant temperature. In the current study, $\langle m_z \rangle = 1.0$ for temperatures above 1022 K (749 °C), $\langle m_z \rangle = 0.7$ for temperatures below 955 K (682 °C), and a linear temperature dependence $\langle m_z \rangle = 1 - 0.3(749 - T)/67$ with T in degrees Celcius was found between 1022 K and 955 K (749 °C and 682 °C). M_s is calculated using the method proposed by Arrott and Heinrich.[23] η can be expressed as $\eta = (1-f)\eta^P + \eta^M$ with $\eta^P = 0.5$ for spherical magnetic particles and $\eta^M = \frac{2}{\pi}\arctan\left(\frac{L_z}{L_y}\right)$ determined by the sample dimensions perpendicular to the neutron beam.[24] Hence, the ferrite volume fraction can be determined.

The correlation function ξ, which is proportional to the correlation length of $\left|\vec{B}(\vec{r})\right|^2$ along the neutron beam, measures the size of the magnetic particles. Assuming that there are no correlations between $\Delta B_i(\vec{r})$ and $\Delta B_j(\vec{r})$ ($i \neq j$) along the neutron path, the relation between the correlation function and the determinant of the depolarization matrix can be expressed as $\xi = -\frac{\ln\left(\det\left(\hat{D}\right)\right)}{2cL_x}$. The effective radius of the magnetic particle that characterizes the average particle size δ is related to the correlation function ξ as

$$\delta = \frac{3c_3\xi}{2f(\mu_0 M_s)^2\left(1 - c_2c_3\langle m_z\rangle^2\right)}, \qquad [4]$$

where the constants c_2 and c_3 are calculated according to Reference 18. For a given particle size distribution, the average particle size δ corresponds to $\delta = \frac{\langle R^4\rangle}{\langle R^3\rangle}$ where R is the particle radius.[18] The validity of the analysis was recently evaluated by simulated particle size distribution.[19] The influence of the particle size distribution was characterized in detail. The previous simulations confirm that Eq. [4] provides a reliable estimate for the ferrite grain size. More detailed information about the 3DND theory can be found elsewhere.[16,17,22]

Steel samples for the 3DND measurements with dimensions $L_x \times L_y \times L_z = 1.5 \times 15 \times 100$ mm^3 were cut from a cold-rolled steel sheet ($1.5 \times 150 \times 200$ mm^3) provided by Arcelor Mittal. The middle area ($\Delta L_y \times \Delta L_z = 15 \times 20$ mm^2) of the sample plate was thinned down to 0.4 mm by spark wire erosion. The chemical composition of the steel sample is given in Table I. The 3DND experiments were performed on the PANDA instrument at the nuclear reactor at the Reactor Institute Delft using a polarized neutron beam with a fixed wave wavelength of 2.06 Å and a spread of about 2 pct. The degree of polarization of the empty beam is 98 pct. The samples were mounted in a sample holder sandwiched by two BN blocks. Three K-type thermocouples were welded onto the sample with an identical spacing to monitor the temperature homogeneity along the vertical axis of the sample. The sample was mounted into a furnace, which was placed on the PANDA instrument, under a vacuum environment (with a pressure $< 10^{-3}$ Pa). In the current study, neutron beam is in the x direction, and the applied magnetic field B_{appl} is along the z direction. During the time-dependent 3DND experiments, the applied magnetic field was $B_{appl} = 6.2$ mT.

In situ 3DND measurements were carried out to investigate the microstructure evolution in the sample during cycling between T_1 and T_2 in the γ/α two-phase region. The sample was first annealed at 1073 K (800 °C) for at least one hour and subsequently cooled to T_1 at a rate of 3 K min^{-1}. After holding at T_1 for 20 minute in order to reach a (quasi-)equilibrium state, the temperature was raised to T_2 and lowered back to T_1 and cycled between these values at a constant rate. After a preset number of cycles, the sample was cooled down to room temperature. During the test, the temperature difference over the sample region probed by the neutron beam was within 2 K. The cycling temperatures and the corresponding equilibrium ferrite fraction calculated with Thermo-Calc software using the TCFE8 database are given in Table II. The sample composition and the cycling temperatures of the Fe-C-2.06 wt pct Mn alloy are shown in the phase diagram in Figure 1. The cycling temperatures were chosen such that the equilibrium ferrite fraction is not too small to form a significant amount of the ferrite phase and is not too large to avoid extensive hard impingement of the ferrite grains. Therefore, the cycling temperatures were chosen to show an equilibrium ferrite fraction between 0.2 and 0.6. The cycling temperature window was set to be constant $\Delta T = 20$ K. As the ferrite formation in this steel is relatively slow according to previous studies,[2,7] we chose a relatively slow cycling rate to ensure that a sizable variation of the ferrite fraction can be observed. As neutron experiments are rate limited too, this low cycling rate matches the relatively long measurement times required for the 3DND measurements: for the current installation 45 seconds were required to complete the determination of a whole depolarization matrix. Figure 1 shows that the temperature is cycled across the A_{e3} under para-equilibrium condition (para-A_{e3}) for the tests of S740 and S750, while for the other tests, the temperature is cycled below para-A_{e3} and above the NPLE/PLE transition temperature between negligible partitioning local equilibrium (NPLE) and partitioning local equilibrium (PLE). The ferromagnetic Curie temperature of the sample is determined from the 3DND measurements as $T_C = 1034$ K (761 °C). Micrographs of the samples after the multicyclic partial transformation 3DND measurements were taken to evaluate the final ferrite grain size. To corroborate the

Table I. The Chemical Composition of the Studied Steel (Weight Percent)

C	Mn	Si	P	Al	N	S
0.247	2.060	0.098	0.023	0.021	0.0033	< 0.002

Table II. The Cyclic Experimental Conditions

Experiments	T_1 (K)	f_{eq}^{α} (T_1)	T_2 (K)	f_{eq}^{α} (T_2)	$\langle T \rangle$ [K (°C)]	ΔT (K)	Cycling Rate (K min^{-1})
S720A	983	0.537	1003	0.417	993 (720)	20	1
S720B	983	0.537	1003	0.417	993 (720)	20	2
S730	993	0.482	1013	0.341	1003 (730)	20	1
S740	1003	0.417	1023	0.253	1013 (740)	20	1
S745	1008	0.381	1028	0.204	1018 (745)	20	1

Characteristic temperatures are ortho-A_{e3} = 1045 K (772 °C), para-A_{e3} = 1020 K (747 °C), NPLE/PLE = 954 K (681 °C), A_1^- = 939 K (666 °C) and T_C = 1034 K (761 °C).

3DND results, rectangular samples with dimensions of 1.5 × 1.5 × 10 mm^3 were heat treated in a DIL805D/T dilatometer with the same temperature profiles as used in the 3DND experiments, but quenched at various stages during multicycling. The samples were etched with 2 pct nital to distinguish between the ferrite and the martensite that was transformed from the austenite during quenching. Both optical and electron microscopy techniques (JEOL JSM 6500F) were used to examine the microstructures of the quenched samples. The ferrite volume fraction was determined using the point-counting method. The 3D ferrite grain radius R_{3D} was derived from the 2D spherical equivalent radius R_{2D} with $R_{3D} = 4R_{2D}/\pi$.[25]

III. RESULTS

A. *Transformation Kinetics in the Whole ND Experiment*

Figure 2 shows the polarization rotation angle φ and the determinant of the depolarization matrix $\det(\hat{D})$ derived from the 3DND data as a function of the temperature for cycling between 993 K and 1013 K (720 °C and 740 °C). The corresponding ferrite volume fraction f_α and average grain radius δ are presented in Figure 3. In addition to the experimentally determined rotation angle measured with the 3DND, the rotation angle for the ortho-equilibrium ferrite fraction has been calculated with Eq. [3] and is shown in Figure 2(b). Figure 3(b) compares the measured and equilibrium ferrite fractions calculated under ortho-equilibrium, para-equilibrium (PE) and negligible partitioning local equilibrium (NPLE) using the Thermo-Calc. During continuous cooling from the fully austenitic state at 1073 K (800 °C), an increase in rotation angle and a decrease in polarization were observed at 1034 K (761 °C), (*i.e.,* the Curie temperature), which suggests that the ferrite started to form at or above this temperature. As shown in Figure 3(b), the presence of ferrite could be confirmed from 1034 K (761 °C) onwards. The values of δ at the earliest stage of ferrite formation are not shown in Figure 3(c). This is because both the ferrite fraction and the derived correlation function are small, resulting in large uncertainties in δ.

During the cooling step and the isothermal holding [20 minutes at T = 993 K (720 °C)], the rotation angle grows until the corresponding ferrite fraction has reached a constant value of $f_\alpha \approx 0.20$. This experimental fraction is still far away from the ortho- or para-equilibrium values predicted from thermodynamics. As the ferrite under NPLE is predicted to form only below 954 K (681 °C), the NPLE condition is not likely to be triggered until the temperature is well below the NPLE/PLE transition temperature. In the cycling region, φ goes up and down with the decreasing and increasing temperatures, while $\det(\hat{D})$ varies in an opposite sense. Over the successive cycles, both the ferrite fraction and the average ferrite grain size increase with respect to the starting moment of the cycling. However, the ferrite fraction after 27 cycles remains below the ortho-equilibrium value, whereas the amplitude of the variation in ferrite fraction during cycling is much smaller than that of PE, indicating a slow transformation kinetics under this condition. Upon further cooling, the ferrite fraction increases, while the derived magnetic particle radius δ decreases. This does not necessarily reflect a decrease in the real grain size, but is probably due to the formation of magnetic multidomains within one grain. Especially, the formation of pearlite in the low-temperature region entered during the slow final cooling stage after the end of the cycling enhances the formation of magnetic domain walls inside individual grains. Moreover, at this stage, the ferrite grains grow more anisotropic due to the higher chance of soft and hard impingements, which compromises the assumption that ferrite grain are quasi-spherical. As a result, according to Eq. [4] (which assumes that ferrite grains remain spherical at all times), the grain size may lead to some deviations in the 3DND estimate of the ferrite grain size in the later stage of the transformation. As shown in Figure 4, the micrograph of this sample indicates that about 25 pct of pearlite is present after cooling at the end of the partial transformation cycles. The metallographically determined final ferrite grain radius is about 5 ± 1 μm, which is comparable to the δ = 4.6 μm obtained at the end of the cycling at 1003 K (720 °C). The value of δ = 3.1 μm obtained at 923 K (650 °C) is, however, significantly lower, as shown in Figure 3(c). This indicates that the decrease of δ in the final cooling stage after cycling is not reflecting the decrease of the ferrite grain size, but caused by the formation of magnetic multidomains in individual ferrite grains.

As shown in Figure 5, the transformation kinetics in the other cyclic experiments shows a similar behavior. All transformations are detectable below the Curie

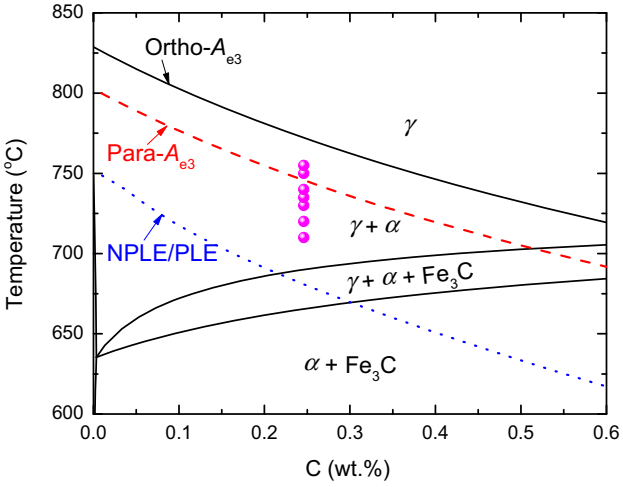

Fig. 1—Phase diagram of Fe-C-2.06 wt pct Mn steel with the composition and the cycling temperatures studied shown as solid circles. The phase boundaries calculated under ortho-equilibrium conditions are shown as solid lines. The A_{e3} line calculated under para-equilibrium is shown as dashed line, while the dotted line indicates the NPLE/PLE transition temperature between negligible partitioning local equilibrium (NPLE) and partitioning local equilibrium (PLE).

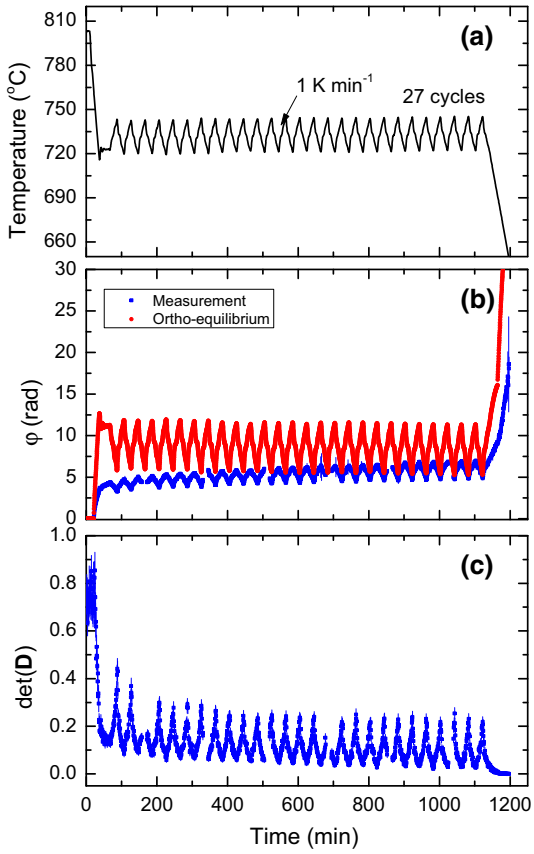

Fig. 2—The temperature profile (*a*) of the cycling experiment between 993 K and 1013 K (720 °C and 740 °C) for sample S730. Derived 3DND parameters: (*b*) rotation angle φ and (*c*) determinant of depolarization matrix $\det(\mathbf{D})$ as a function of time.

temperature of 1034 K (761 °C). The transformation proceeds with a relatively high speed during the first cooling stage, and then slows down in the isothermal stage. The ferrite fraction is enhanced by a decrease in the minimum transformation temperature, and the ferrite grain size grows to higher values in samples that are cycled at lower temperature ranges. For cycling tests between 1003 K and 1023 K (730 °C and 750 °C, S740) and 1008 K and 1028 K (735 °C and 755 °C, S745), the ferrite fraction is nearly the same, and also the ferrite grain size is changing around a comparable value of about 2.5 μm. By decreasing the cycling temperature range, the average ferrite grain size δ increases, and the change in each cycle is more distinct. The rates of changes in both the ferrite fraction and the ferrite grain size are slightly more enhanced at a higher cycling rate, as can be seen the cycling tests between 983 K and 1003 K (710 °C and 730 °C) at a rate of 2 K min^{-1} (S720B) compared to that at a rate of 1 K min^{-1} (S720A).

The ferrite fraction and the average ferrite grain size determined by imaging analysis on the quenched samples are also plotted in Figures 5(b) and (c) to compare with the 3DND results. The data are in good agreement with each other; only f_α is slightly smaller for the image analysis than for the 3DND. Figure 6 shows the micrographs of the quenched samples where both the ferrite and the martensite that was transformed from the austenite during quenching, are present.

B. *Transformation Kinetics and Grain Size Evolution During Individual Cycles*

A closer look at the transformation behavior during individual cycles is shown in Figure 7 for cycling between 993 K and 1013 K (720 °C and 740 °C, S730) and in Figure 8 for cycling between 983 K and 1003 K (710 °C and 730 °C, S720A), respectively. As explained in References 26, the kinetics in initial cycling stage is most relevant to the physical properties of the interface, *e.g.*, interfacial mobility and partitioning of substitutional alloy elements, as there is less chance of soft or hard impingement. Therefore, we show the details of the first several cycles in Figures 7 and 8.

A net increase in ferrite fraction after heating and cooling in each cycle is observed in both Figures 7 and 8. The transition from decreasing f_α during heating to increasing f_α during cooling coincides with the moment of switching from heating to cooling and *vice versa*. Little inverse transformation, where the transformation does not proceed in line with the temperature change, is seen. However, the average grain size shows a more complicated behavior than f_α. In Figure 7, δ monotonically decreases and increases over changing temperature in the first cycle followed by more variations in the following cycles. By looking at the overall changes in each heating and cooling segments for each cycle, one finds there is a decrease of δ in the heating part and an increase of δ in the cooling part, which is in line with the change of f_α as one would generally expected. A larger variation in δ can be seen in Figure 8 for the cycling experiment between 983 K and 1003 K (710 °C and 730 °C). The δ even partially tends to increase as

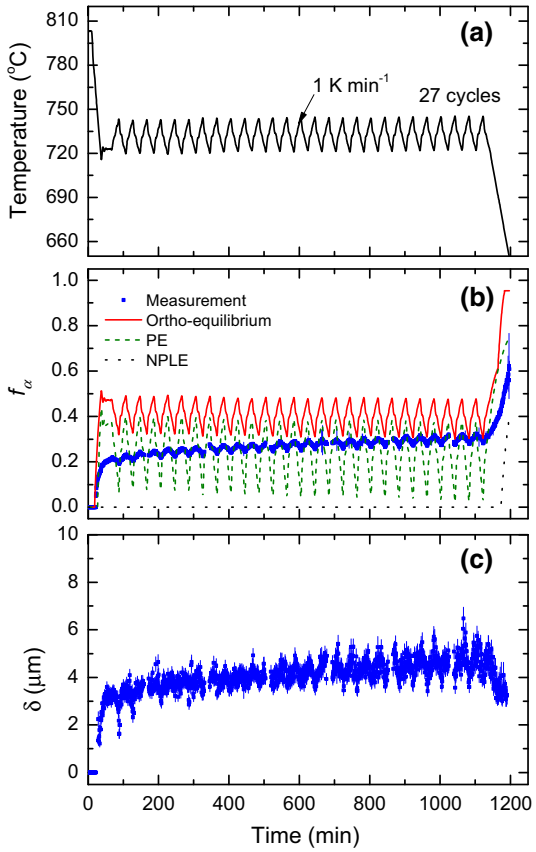

Fig. 3—The temperature profile (*a*) of the cycling experiment between 993 K and 1013 K (720 °C and 740 °C) for sample S730, (*b*) ferrite volume fraction f_α, and (*c*) average ferrite grain radius δ derived from the 3DND measurements shown in Fig. 2 as a function of time. The equilibrium ferrite fractions calculated under ortho-equilibrium, PE, and NPLE are also shown in (b) for comparison.

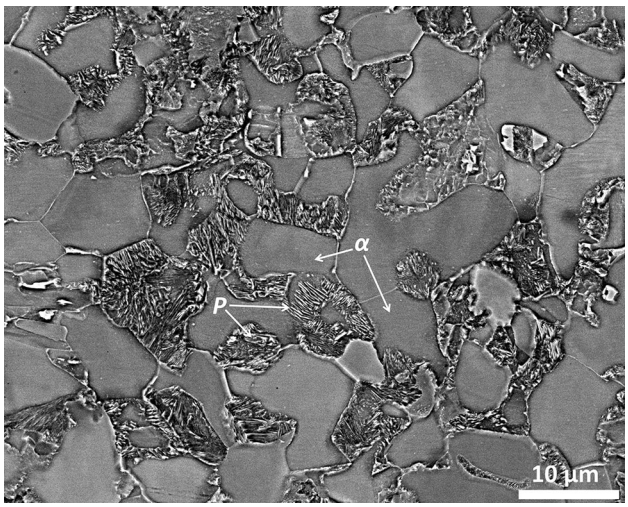

Fig. 4—SEM graph of the S730 sample showing ferrite (α) and pearlite (P) after the 3DND measurement.

temperature goes up and decrease as temperature cools down. This unexpected change of δ is not accidental because a similar behavior of δ is also found in the

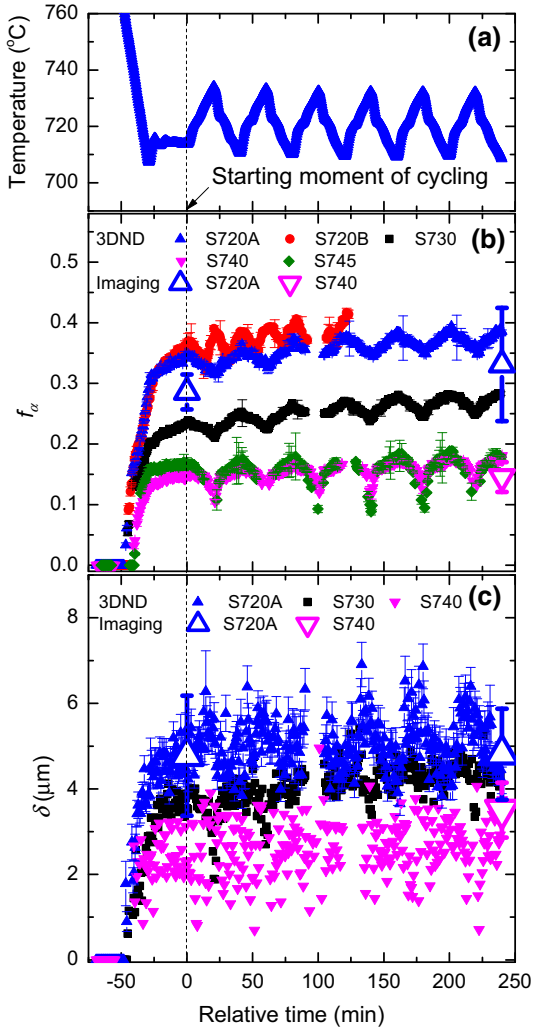

Fig. 5—(*a*) The temperature profile of the cycling experiment between 983 K and 1003 K (710 °C and 730 °C) at a rate of 1 K min^{-1} (sample S720A), which resembles the temperature profiles of all other tests. Comparison of (*b*) f_α and (*c*) δ derived from the 3DND measurements for the first 6 cycles. The reference time (t = 0) is selected to be the start of the cycling. Only the error bars of grain radius for the cycling experiment between 983 Kand 1003 K (710 °C and 730 °C) at a rate of 1 K min^{-1} (sample S720A) are shown for clarity in (b). The grain radius for the other tests show comparable error bars. For clarity, the grain size is only shown for the S720A, S730, and S740 samples. The values for f_α and δ derived from image analysis on quenched samples are also plotted in (b) and (c).

cycling experiment between 983 K and 1003 K (710 °C and 730 °C) at a higher rate of 2 K min^{-1}. At first thought, one may think this is a contradictory trend because an increase in f_α must be associated with an increase in grain size if there are no new nuclei formed. However, it should be noted that the δ derived from the 3DND technique is a measurement of the average grain size, and its estimate is dominated by the bigger grains as $\delta = \langle R^4 \rangle / \langle R^3 \rangle$. For cycling between 983 K and 1003 K (710 °C and 730 °C), a bigger grain size exists in the initial cycling stage compared to the other cycling experiments (see Figure 4(b)), which implies the concentrations of C and Mn are more likely to be higher in

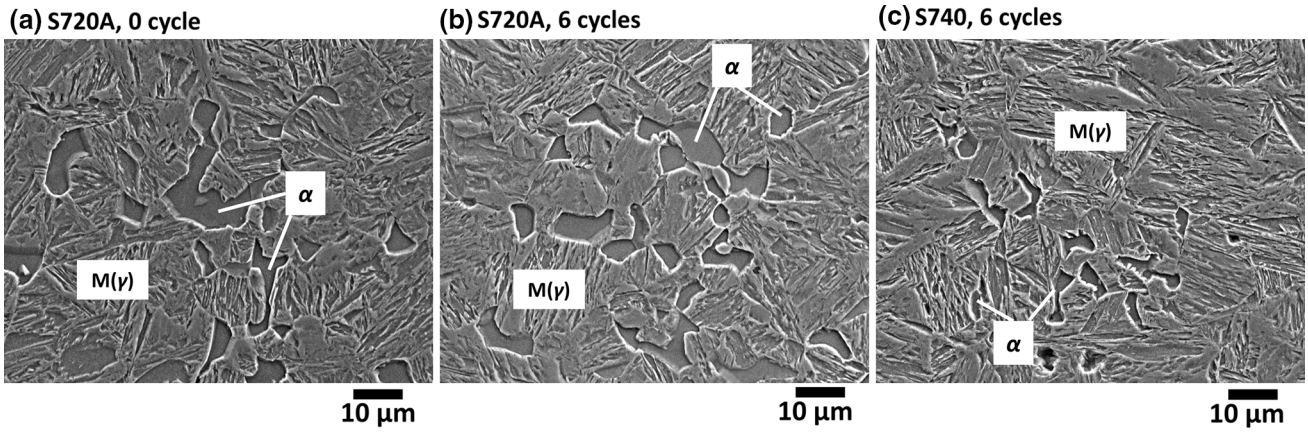

Fig. 6—Secondary electron images of the samples quenched after (*a*) 0 cycle and (*b*) 6 cycles for S720A, and (*c*) 6 cycles for S740. M(γ): martensite; α: ferrite.

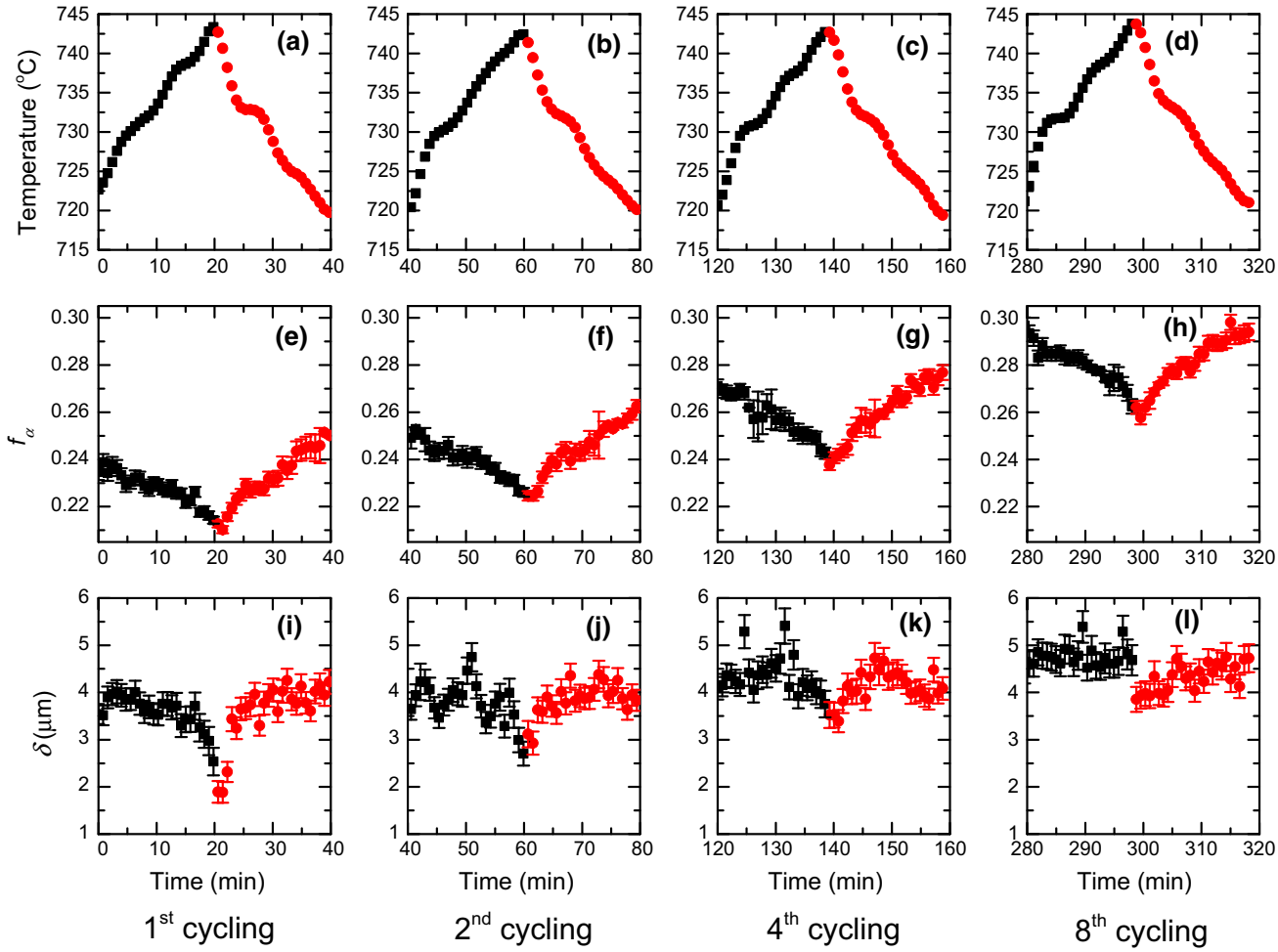

Fig. 7—Measured f_α and δ values as a function of time between 993 K and 1013 K (720 °C and 740 °C) at a rate of 1 K min^{-1} (S730) for individual cycles: (*a*, *e*, *i*) the first cycle; (*b*, *f*, *j*) the second cycle; (*c*, *g*, *k*) the fourth cycle; and (*d*, *h*, *l*) the eighth cycle. The reference time $t = 0$ indicates the start of the cycling. The data obtained during heating are shown in black squares, and during cooling in red circles (Color figure online).

the untransformed austenite. When the temperature change switches direction, the bigger ferrite grains respond slower because of the higher concentrations of solute Mn atoms at the surrounding interfacial boundaries of the larger grains. This slower response may cause the hysteretic response of δ to the temperature

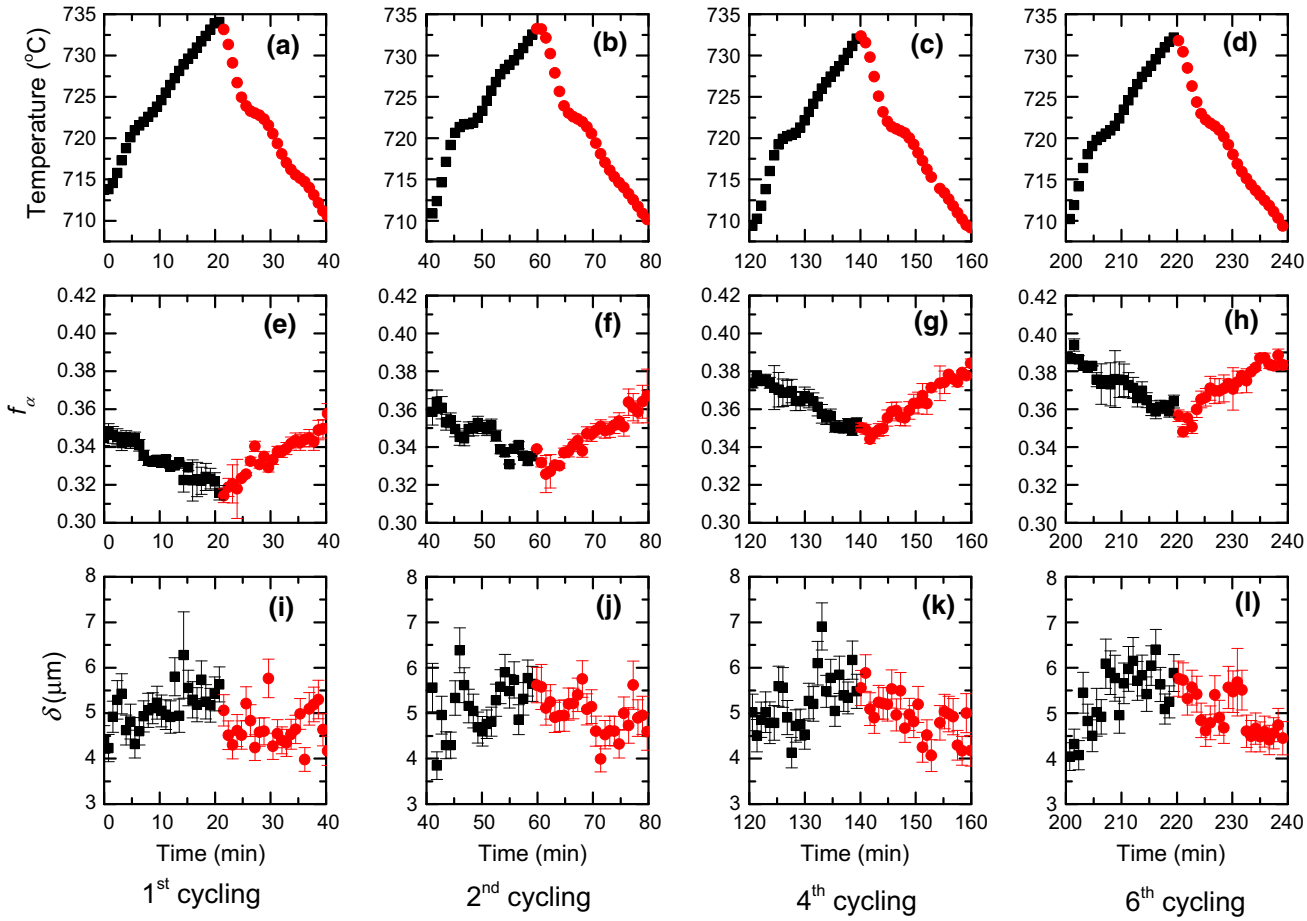

Fig. 8—Measured f_α and δ values as a function of time between 983 K and 1003 K (710 °C and 730 °C) at a rate of 1 K min^{-1} (S720A) for individual cycle: (*a*, *e*, *i*) the first cycle; (*b*, *f*, *j*) the second cycle; (*c*, *g*, *k*) the fourth cycle; and (*d*, *h*, *l*) the sixth cycle. The reference time $t = 0$ indicates the start of the cycling. The data obtained during heating are shown in black squares, and during cooling in red circles (Color figure online).

change, which can result in the more disordered change of δ shown in Figure 8.

For each heating and cooling part of an individual cycle, we calculate the average rate of change for the ferrite fraction $\langle df_\alpha/dt \rangle$ and the ferrite grain size $\langle d\delta/dt \rangle$, which are summarized in Table III. A positive sign indicates that the austenite transforms to ferrite, and a negative sign indicates that ferrite transforms to austenite. The experimental data suggest that the interfacial migration is very sluggish, which was also found in several other studies on isothermal transformations in steels with similar Mn concentration.[2,7,27–29] As mentioned earlier, this tendency for f_α is in line with the temperature change for all cycling tests, while a more disordered behavior is found for δ in the cycling experiments between 983 K and 1003 K (710 °C and 730 °C). To quantify the net increases in f_α and δ for an increasing number of cycles, we plot the averages of f_α and δ for the heating and cooling parts of each cycle as a function of the cycle number in Figure 9. The rates at which f_α and δ increase are clearly found to increase for a decrease in cycling temperature for most of the cycling experiments, except for the rate of δ during cycling between 993 K and 1013 K (720 °C and 740 °C, S730) which is even larger than that during the cycling between 983 K and 1003 K (710 °C and 730 °C, S720A). Although there is a considerable variation in behavior for δ when cycling between 1008 K and 1028 K (735 °C and 755 °C, S745) compared to the cycling between 1003 K and 1023 K (730 °C and 750 °C, S740), the net increase in f_α is very limited.

Since the interface migrates slowly in the samples of this study, the ferrite fraction is still far from equilibrium at the end of the cycling (see Figure 3, for example). There are two coupled effects in the cycling behavior of this 2.1 wt pct Mn steel: (i) the intrinsic cycling behavior which moves the γ/α interface back and forth; (ii) the net increase in f_α and δ over continued cycling. In particular, the second phenomenon makes the cycling behavior quite different from a previously reported study[11] on a lean, low Mn steel (Fe-0.023C-0.17Mn in wt pct).

C. *Comparison to DICTRA Simulations*

To further analyze the cycling behavior for the current steel, the experimental transformation kinetics is compared to the kinetics predicted by DICTRA (linked to the TCFE7 and MOB2 databases)

Table III. The Average Rate of Change df_α/dt and $d\delta/dt$ During Heating and Cooling Segments of the Studied Cycles

	$\langle df_\alpha/dt\rangle$ ($\times 10^{-5}$ s^{-1})		$\langle d\delta/dt\rangle$ ($\times 10^{-3}$ μm s^{-1})		$\left\vert D^{\text{int}}_{\text{Mn}}/v\right\vert$ (nm)		$\left\vert \frac{D^{\text{int}}_{\text{Mn}}}{v}\middle/\frac{C^{\gamma*}_{\text{Mn}}-C^{\alpha*}_{\text{Mn}}}{C^{\gamma*}_{\text{Mn}}-C^{0}_{\text{Mn}}}\right\vert$ (nm)	
Experiments	Heating	Cooling	Heating	Cooling	Heating	Cooling	Heating	Cooling
S720A	− 2.3 (5)	3.2 (2)	1.0 (3)	− 0.7 (3)	5.2 (9)	7.4 (8)	4.1 (9)	5.9 (9)
S720B	− 5.8 (9)	7.6 (2)	2.9 (7)	− 2.4 (6)	1.8 (6)	2.2 (6)	1.3 (6)	1.6 (6)
S730	− 2.7 (5)	3.2 (6)	− 0.5 (4)	0.5 (4)	13.9 (9)	14.0 (9)	9.2 (9)	9.2 (9)
S740	− 3 (1)	3 (1)	− 1.8 (8)	1.3 (9)	5.2 (9)	7.2 (9)	3.1 (9)	4.2 (9)
S745	− 5 (2)	5 (2)	− 2.0 (6)	1.8 (6)	5.4 (8)	6.0 (9)	5.3 (8)	5.8 (9)

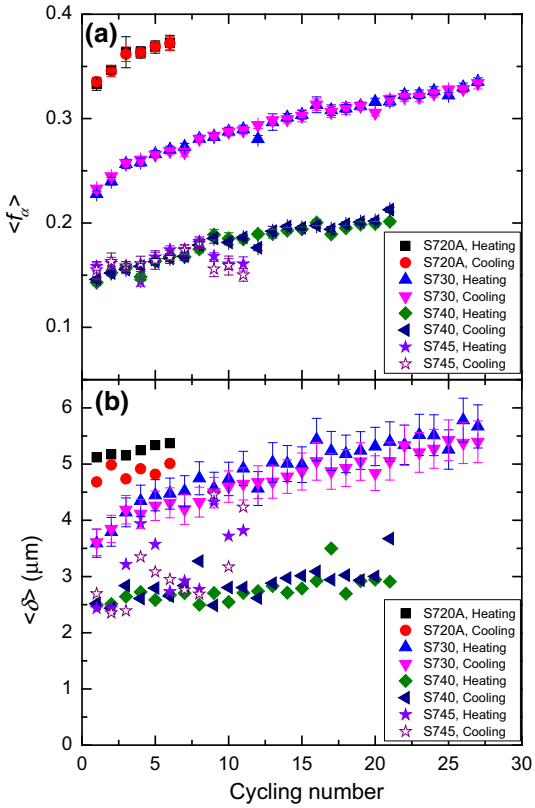

Fig. 9—Average (*a*) ferrite fraction f_α and (*b*) ferrite particle radius δ obtained for heating and cooling segments in individual cycles as a function of the cycling number.

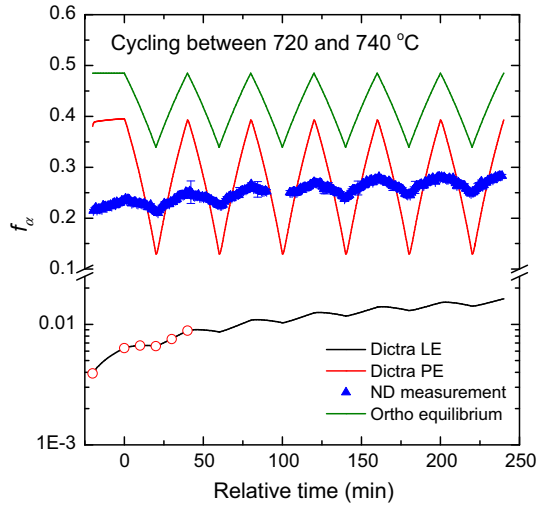

Fig. 10—Ferrite fraction f_α during cycling between 993 K and 1013 K (720 °C and 740 °C, S730) derived from the 3DND (triangles) compared to the calculated values derived from DICTRA simulations imposing local equilibrium (LE) and para-equilibrium (PE) conditions. For reference, the ortho-equilibrium is also indicated (Color figure online).

simulations.[30] In the simplified (1-D) DICTRA simulation, we start with a planar austenite phase with a length of 10 μm and a thin ferrite phase of 10 nm growing from one side. The same temperature profile as used in 3DND experiments is applied to the simulation. The starting composition of the bulk austenite is Fe-0.247C-2.06Mn (wt pct). Two interfacial conditions are assumed: local equilibrium (LE) and para-equilibrium (PE).[30]

Figure 10 shows the comparison of the ferrite fraction derived from 3DND for cycling experiment between 993 K and 1013 K (720 °C and 740 °C, S730) and the ferrite fraction derived from the DICTRA simulations. The ortho-equilibrium values of ferrite fraction calculated from phase diagrams are also shown. The experimental f_α is located in between the DICTRA predictions under LE condition and ortho-equilibrium, while it intertwines with the predictions under PE condition. None of the simulations directly corresponds to the transformation kinetics derived from the 3DND experiment. This is not surprising as Mn diffusion normally shows an intermediate behavior located between the LE and PE predictions.[29,31,32] The tendency for f_α is qualitatively consistent with the simulation under LE, although the absolute values of f_α differ more than one order of magnitude. Similar to the 3DND results, the simulations under LE also show a slight increase of f_α in the isothermal stage followed by a cyclic decrease and increase. This behavior is not found in the simulations under PE.

Regarding the cyclic behavior of f_α, shown in both the 3DND experimental data and the simulation results under LE, one question arises: why does f_α decrease during heating in each cycle, while the fraction is still far away from its ortho-equilibrium value? One would expect that f_α does not decrease during heating, but continues to increase with a slower rate than that during cooling, which is thermodynamically favored. The observed behavior is however related to the relative speed of the Mn diffusion and the interfacial velocity.

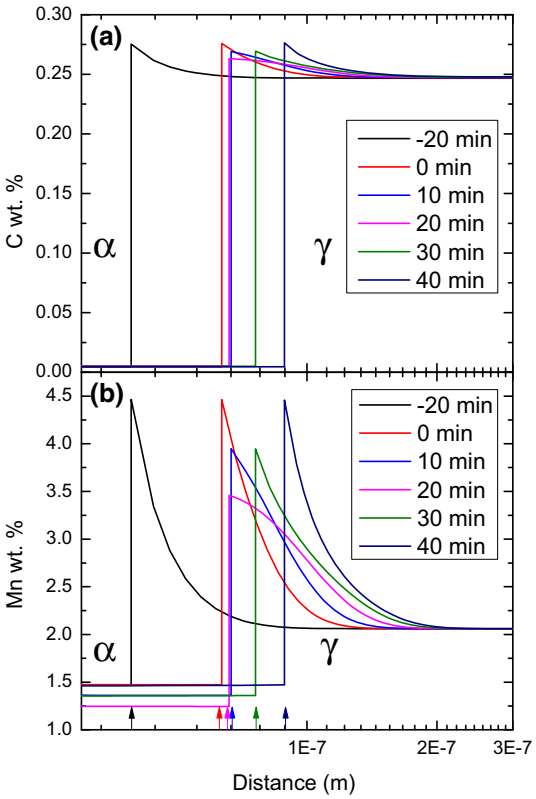

Fig. 11—(*a*) C and (*b*) Mn diffusion profiles derived from DICTRA simulations under LE conditions with arrows indicating the position of the interface. The times correspond to those indicated by the red circles in Fig. 10.

Figure 11 shows the diffusion profiles of C and Mn for the first cycle for the simulation under LE, which is assumed to qualitatively represent the development of the C and Mn profiles in the 3DND experiment. After the primary cooling, diffusion spikes in C and Mn are formed at the interface and move forward until the start of the heating in the first cycle. During heating, the interfacial concentrations of C and Mn are decreasing, which drives the solutes into the austenite or diffuse back to the ferrite. In the early stages of heating, the solutes are still able to diffuse into austenite, whereas with the increasing temperature, more and more solutes need to be diffused out, which decreases the interfacial concentration gradients in austenite and ultimately change the direction of the concentration gradient. This change triggers a reversal of the direction in which the transformation proceeds. However, since only part of the solutes in the original spike can diffuse back into the ferrite during heating, the interface moves back to form ferrite, resulting in a weaker back transformation than the forward transformation during cycling. This is why we also observed a net increase in f_α over cycling. The reversal in transformation direction is essentially attributed to the partitioning of Mn and the slow diffusion rate of Mn in austenite (or inside the interface depending on the length scale of the Mn diffusion length). At these temperatures, $D^{\gamma}_{\mathrm{Mn}}/D^{\gamma}_{C} \approx 10^{-6}$ and as a result, there is no depletion of Mn at the ferrite side. The reversal of the transformation direction due to Mn diffusion was previously analyzed by Vitek *et al.*[33] They showed that a reversal may happen when a transition from the PE mode to the LE mode occurred during an isothermal at 983 K (700 °C) of Fe-0.1C-3Mn (wt pct). They did however not find experimental evidence from dilatometer measurements. With our 3DND measurements during cycling transformations, we experimentally observed a reversal of the transformation direction, which is probably caused by the diffusion of the substitutional element.

IV. DISCUSSION

A. *The Absence of New Nucleation During Cycling*

The 3DND technique provides an unique way to simultaneously measure the ferrite fraction and the average ferrite grain size. Assuming that the ferrite grains are spherical, we can estimate the number density ρ_α of ferrite grains from the following equation:

$$\rho_\alpha = \frac{3f_\alpha}{4\pi\delta^3}. \qquad [5]$$

To clarify the evolution of ρ_α, we plotted the average of ρ_α for the heating and cooling part of each cycle as a function of the cycling number in Figure 12. It is clearly observed that the number density is constant over cycling with fluctuations within the experimental uncertainty. These results are distinct evidence that ferrite nucleation is indeed negligible during the cyclic transformation and that the transformation is therefore only controlled by ferrite growth. In Figure 12(b), there is a slight monotonic decrease of ρ_α over cycling. This suggests that in this cycling experiment some coarsening of ferrite grains is taking place.

For the cycling data of Figure 12(b), plotting $\delta^3 - \delta_0^3$ as a function of time in Figure 13(a) clearly shows a linear relationship $\delta^3 - \delta_0^3 = kt$ with a coarsening rate of $k = 0.129(4)\ \mu\mathrm{m}^3\ \mathrm{min}^{-1}$. Figure 13(b) directly shows that the number of ferrite grains decreases over time, confirming the coarsening behavior at this temperature range.

For cycling at other temperatures, the ferrite grain coarsening is not significant as ρ_α is constant during the whole cycling process as shown in Figure 12. The reduction of ferrite grain boundary area, *i.e.,* coarsening, can take place by full hard impingement on the austenite grain boundaries and/or coalescence of ferrite grains.[34,35] The significance of coarsening is most directly related to the spacing of the ferrite grains, the degree of transformation with respect to the equilibrium and the ferrite grain boundary mobility. These parameters are now given in Table IV for the cycling experiments. For cycling at the highest temperatures (S740 and S745), coarsening is found to be not very considerable due to the large difference between the formed ferrite fraction and the equilibrium fraction $\left(\left(f_\alpha^{\mathrm{eq}} - f_\alpha\right)/f_\alpha^{\mathrm{eq}} > 0.45\right)$, although the grain spacing is smaller. For cycling at the lowest temperatures (S720A), the negligible coarsening is probably due to the larger

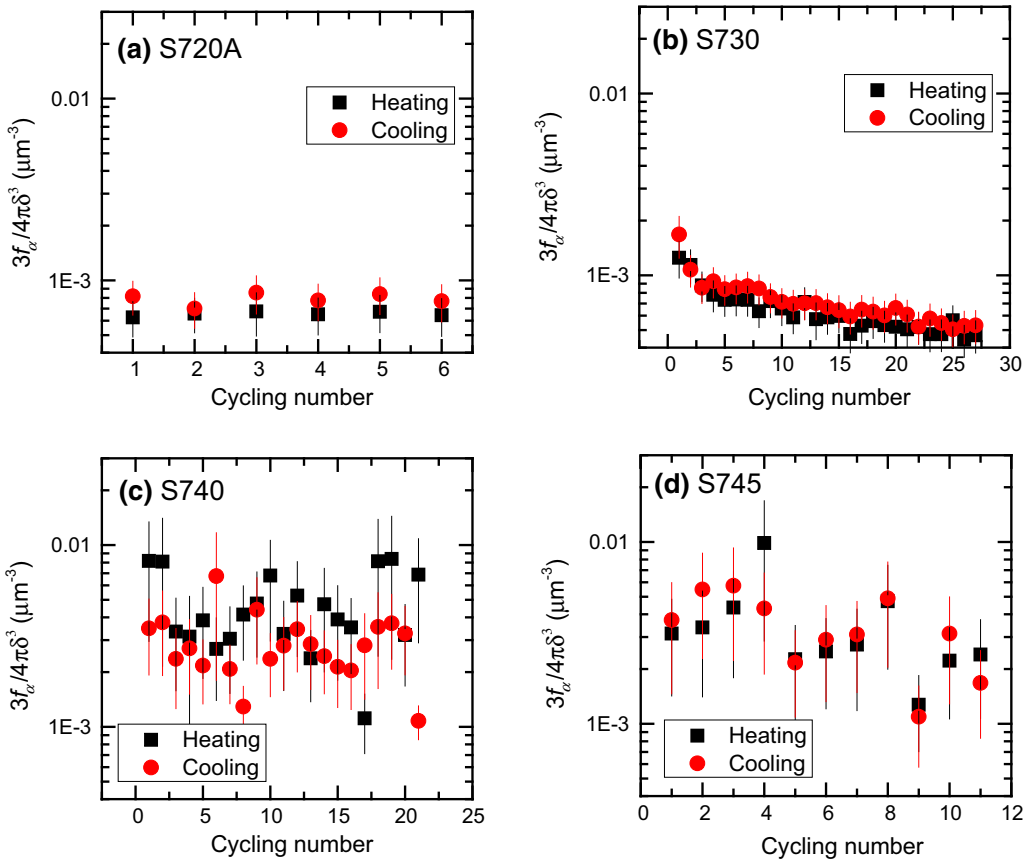

Fig. 12—Evolution of the number density of ferrite grains $3f_\alpha/4\pi\delta^3$ as a function of the cycling number for cycling experiments. (*a*) S720A, (*b*) S730, (*c*) S740, and (*d*) S745. The sample name indicates the average temperature during cycling with a temperature span of $\Delta T = 20$ K.

spacing between ferrite grains and a decrease in diffusivities at lower temperature, which slows down the coarsening kinetics.

B. *Interfacial Migration During Cycling*

The partial cyclic approach, now experimentally proven to occur in the absence of new nucleation, provides a direct insight into the interaction between the interfacial migration and the substitutional elements. In the present 3DND study of Fe-0.25C-2.1Mn (wt pct), the interface migrates slowly back and forth with a net increase in both the ferrite fraction and the ferrite grain size over cycling. Ferrite is shown to be able to transform back from the austenite as a result of the diffusional flux balance of Mn between ferrite and austenite during each cycle, even though the ferrite fraction is far from equilibrium. This progressive migration into austenite over cycling, coupled with the cyclic interfacial migration, indicates that the migration of the interface is predominantly controlled by the Mn diffusion front that stays in contact with the moving interface. This situation differs from the cyclic behavior in Fe-0.023C-0.17Mn (wt pct),[11] where the interface can migrate by 'cutting' through the Mn diffusion spike and can leave that spike behind. The Mn diffusion spike in the present alloy always exists in the vicinity of the interface and its length scale is expected to be longer than the width of the interface. This interaction between the interfacial migration and Mn diffusion is controlled by three factors: (i) the diffusivity of Mn in austenite D_γ^{Mn}, (ii) the velocity of the interface v, (iii) the interfacial concentrations. These three factors together control the length scale L of the Mn diffusion spike. In general, L can be expressed as[37]

$$L = \frac{D_{\mathrm{Mn}}}{v} \Big/ \frac{c_{\mathrm{Mn}}^{\gamma *} - c_{\mathrm{Mn}}^{\alpha *}}{c_{\mathrm{Mn}}^{\gamma *} - c_{\mathrm{Mn}}^{0}}, \qquad [6]$$

where c_{Mn}^0 is the nominal concentration of Mn. For isothermal transformations, Coates[38] showed that $L = 2D/v$ and analyzed that interface migrates under LE condition for $L > 5$ nm, while the diffusion zone becomes part of the interface for $L < 5$ nm. Hillert[39] similarly pointed out that the interfacial condition is close to LE for $D/v > 10d$ where d is the atomic distance, whereas interface migrates under PE for $D/v < 0.4d$. As listed in Table III, we calculated the average values of $D_\gamma^{\mathrm{int}}/v$ in the cycling stage, where $D_{\mathrm{Mn}}^{\mathrm{int}} = \sqrt{D_{\mathrm{Mn}}^{\alpha} D_{\mathrm{Mn}}^{\gamma}}$ with $D_{\mathrm{Mn}}^{\alpha} = 0.756 \times 10^{-4} \exp\left(-224.5 \times 10^3 / RT\right)$ and $D_{\mathrm{Mn}}^{\gamma} = 0.178 \times 10^{-4} \exp\left(-264 \times 10^3 / RT\right)$.[40] The calculated value of L obtained from Eq. [6] by assuming an LE interfacial condition is also given. The results suggest that the interface migrates most likely in an intermediate conditions between LE and PE for a

cycling rate of 1 K min^{-1} according to the criteria proposed by Coates[38] and Hillert.[39] This is fully in line with the experimental behavior for f_α, which according to the simulations shows a behavior between the LE and the PE conditions (see Figure 10).

The present study shows that the cyclic interfacial migration is coupled with a net increase in both f_α and δ over cycling. The intrinsic cyclic behavior is weakened and is difficult to capture independently unless these two effects could be decoupled. We attempted to decouple these two effects by subtracting the average for each heating and cooling part from the individual cycles. As shown in Figure 14, the transformation curves for $f_\alpha - f_\alpha$ form a closed loop for each cycle. The loops overlap and therefore reproduce for different cycles. This suggests that the cyclic interfacial mobility can be analyzed in more detail after the effect of progressing migration into austenite is decoupled from the cyclic effect. In Figure 14, we can now also observe a stagnant stage where the interface is quasi-immobile.[11] The formation of this stage is mainly due to Mn partitioning. How this stagnant phase is affected by the cycling rate and concentrations of substitutional elements has been analyzed computationally in detail for low substitutional element concentrations in Reference 41 According to Reference 41, the length of the stagnant stage (measured by temperature difference ΔT where interface is immobile) may become very small or can even disappear for the low heating and cooling rates of 1 K min^{-1} used in the present study. For the current 2.1 wt pct Mn steel, the lengths of the stagnant stage appear to be ΔT = 6 K and 3 K for cycling experiments between 983 K and 1003 K (710 °C and 730 °C, S720A) and 993 K and 1013 K (720 °C and 740 °C, S730), respectively. For cycling experiment between 1003 K and 1023 K (730 °C and 750 °C, S740) shown in Figure 14(c), the interface migrates more sluggishly at the lower temperatures than at the higher temperatures compared to the cycling experiments shown in Figures 14(a) and (b). The area of the loop gives an indication of how strong the Mn partitioning can drag the interfacial migration. As shown in Reference 39, the area of the cyclic loop increases with the increasing Mn concentrations for the same carbon content, and correspondingly, the length of the stagnant stage increases with additions of substitutional elements such as Mn, Ni, and Si. A detailed physical description of the cyclic loop requires further study.

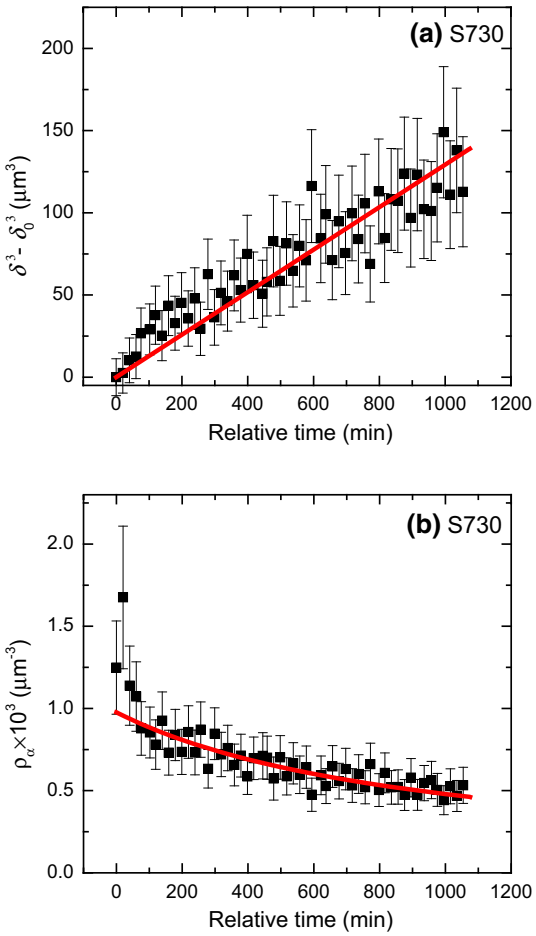

Fig. 13—(*a*) Evolution of $\delta^3 - \delta_0^3$ ('0' denotes the starting moment of cycling) as a function of time t, showing a fit to $\delta^3 - \delta_0^3 = kt$ with a slope of k = 0.129(4) μm^3 min^{-1} for cycling between 993 K and 1013 K (720 °C and 740 °C, S730). (*b*) The corresponding number of ferrite grain as a function of time t, which can be fitted to $\rho_\alpha = \frac{\rho_0}{1+\beta t}$ with ρ_0 = 9.8(4) × 10^{-4} μm^{-3} and β = 1.0(1) × 10^{-4} min^{-1}.

It is widely accepted that the partitioning of substitutional elements like Mn could lead to a stagnant $\gamma \rightarrow \alpha$ transformation upon switching from heating to cooling and *vice versa*. Modeling approaches that take into account the energy dissipation due to the trans-diffusion of substitutional elements inside the interface have been able to predict transformation stasis.[5,42–44] However, as shown in the present study, the length scale of Mn diffusion spike can vary from 1 to 15 nm, which suggests that both the short-range and long-range diffusion of Mn play an important role in the slowing down of the interfacial migration. This provides a

Table IV. The Average Values of Ferrite Grain Spacing $\rho_\alpha^{-1/3}$, Relative Degree of Transformation $(f_\alpha^{eq} - f_\alpha)/f_\alpha^{eq}$ and *bcc* Iron Bulk Diffusivity $D_{bulk}^{Fe,\alpha}$ and Grain-Boundary Diffusivity $D_{GB}^{Fe,\alpha}$ Calculated According to Ref. [36]

Experiments	$\langle \rho_\alpha^{-1/3} \rangle$ (μm)	$\langle (f_\alpha^{eq} - f_\alpha)/f_\alpha^{eq} \rangle$ (–)	$\langle D_{bulk}^{Fe,\alpha} \rangle$ (m^2 s^{-1})	$\langle D_{GB}^{Fe,\alpha} \rangle$ (m^2 s^{-1})
S720A	11.1 (9)	0.26	1.25 × 10^{-17}	5.68 × 10^{-12}
S730	9.5 (7)	0.29	1.77 × 10^{-17}	6.34 × 10^{-12}
S740	6 (2)	0.47	2.51 × 10^{-17}	7.06 × 10^{-12}
S745	6 (2)	0.46	2.97 × 10^{-17}	7.45 × 10^{-12}

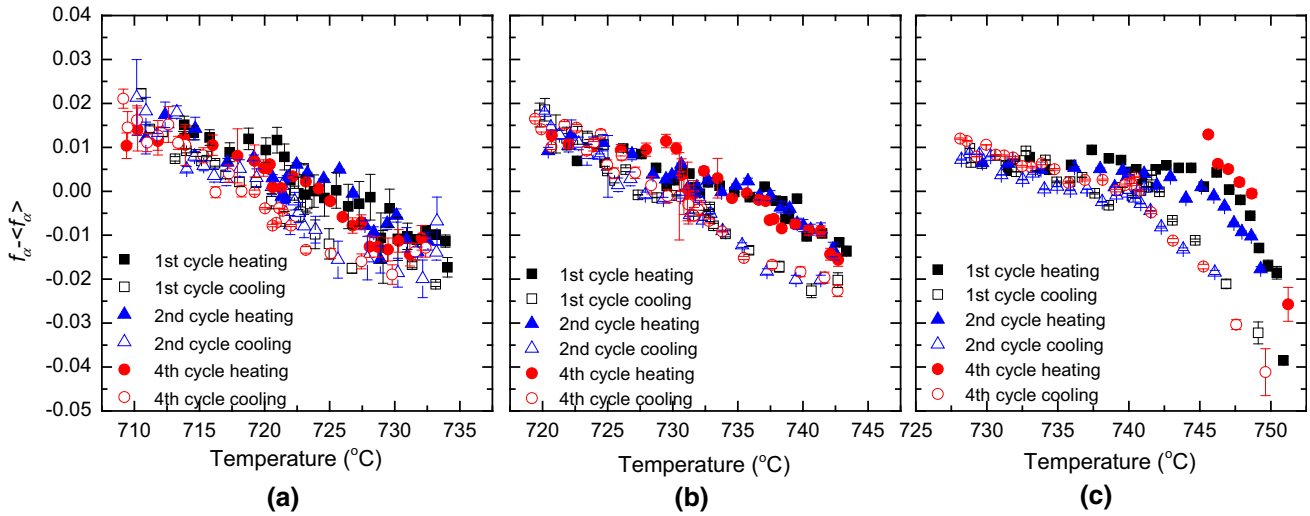

Fig. 14—Cyclic part of the ferrite phase fraction $f_\alpha - \bar{f}_\alpha$ as a function of temperature for the first 4 cycles for (*a*) 983 K and 1003 K (710 °C and 730 °C, S720A), (*b*) 993 K and 1013 K (720 °C and 740 °C, S730), and (*c*) 1003 K and 1023 K (730 °C and 750 °C, S740) at a cycling rate of 1 K min^{-1}.

challenge to quantitatively address the effects of long-range Mn diffusion in the grain and local diffusion inside the interface. The concept of an effective interfacial mobility[13] may still remain a useful approach to account for the long-range of Mn diffusion together with the solute drag theory[44–46] to describe the energy dissipation due to the diffusion inside the interface.

V. CONCLUSIONS

The evolution of the ferrite fraction and the ferrite grain size during slow partial cyclic austenite-ferrite phase transformations in Fe-0.25C-2.1Mn (wt pct) steel has been studied in detail with 3DND experiments. The number density of the ferrite grains was estimated, and the results demonstrate that during cycling additional nucleation is proven to be negligible or even absent. Hence, the current study provides the experimental evidence that cyclic partial transformations indeed can yield direct information on the actual movement of the austenite-ferrite interface and can be free from the effects of simultaneous nucleation. During cycling, the austenite-ferrite interface migrates into the austenite region and back to the ferrite region in each cycle with a net increase in both ferrite fraction and ferrite grain size over multiple cycles; a feature which cannot be captured by 1D (or fixed geometry) simulations of interfacial mobility during solid state phase transformations. The interfacial migration velocity is of the order of 10^{-3} μm/s during cycling. This low value is attributed to Mn partitioning. The length of the Mn diffusion spike is estimated to be 1–15 nm, indicating a probable coexistence of short-range and long-range diffusions. The intrinsic cyclic behavior of the interfacial migration is visible after subtracting the effect of the progressive interfacial migration into austenite. The closing cyclic loops are reproducible and reveal a stagnant stage.

ACKNOWLEDGMENTS

The authors are grateful to Dr. Astrid Perlade at Arcelor Mittal Marzières-lèts-Metz for providing the steel samples, and Prof. Ekkes Brück for fruitful discussion. Haixing Fang acknowledges the support by Hussein Farahani for providing access and guidance to DICTRA software, and the financial support provided by the China Scholarship Council (CSC).

REFERENCES

1. G. Purdy, J. Ågren, A. Borgenstam, Y. Bréchet, M. Enomoto, E. Gamsjager, M. Gouné, M. Hillert, C. Hutchinson, M. Militzer, and H. Zurob: *ALEMI: Metall. Mater. Trans. A*, 2011, vol. 42A, pp. 3703–18.
2. H.S. Zurob, C.R. Hutchinson, Y. Brechét, H. Seyedrezai, and G.R. Purdy: *Acta Mater.*, 2009, vol. 57, pp. 2781–92.
3. E. Novillo, D. Hernández, I. Gutiérrez, and B. López: *Mater. Sci. Eng. A*, 2004, vol. 385, pp. 83–90.
4. A. Phillion, H.W. Zurob, C.R. Hutchinson, H. Guo, D.V. Malakhov, J. Nakano, and G.R. Purdy: *Metall. Mater. Trans. A*, 2004, vol. 35A, pp. 1237–42.
5. H. Chen and S. van der Zwaag: *Acta Mater.*, 2014, vol. 72, pp. 1–12.
6. S.E. Offerman, N.H. van Dijk, J. Sietsma, S. Grigull, E.M. Lauridsen, L. Margulies, H.F. Poulsen, M.T. Rekveldt, and S. van der Zwaag: *Science*, 2002, vol. 298, pp. 1003–05.

7. H. Guo, G.R. Purdy, M. Enomoto, and H.I. Aaronson: *Metall. Mater. Trans. A*, 2006, vol. 37A, pp. 1721–29.
8. Z.Q. Liu, G. Miyamoto, Z.G. Yang, and T. Furuhara: *Acta Mater.*, 2013, vol. 61, pp. 3120–29.
9. C.R. Hutchinson, A. Fuchsmann, and Y. Bréchet: *Metall. Mater. Trans. A*, 2004, vol. 35A, pp. 1211–21.
10. M. Gouné, F. Danoix, J. Ågren, Y. Bréchet, C.R. Hutchinson, M. Militzer, G. Purdy, S. van der Zwaag, and H. Zurob: *Mater. Sci. Eng. R*, 2015, vol. 92, pp. 1–38.
11. H. Chen, B. Appolaire, and S. van der Zwaag: *Acta Mater.*, 2011, vol. 59, pp. 6751–60.
12. H. Chen and S. van der Zwaag: *Metall. Mater. Trans. A*, 2017, vol. 48A, pp. 2720–29.
13. E. Gamsjäger, M. Wiessner, S. Schider, H. Chen, and S. van der Zwaag: *Philos. Mag.*, 2015, vol. 95, pp. 2899–2917.
14. M. Segawa, A. Yamanaka, and S. Nomoto: *Comput. Mater. Sci.*, 2017, vol. 136, pp. 67–75.
15. H. Chen, B. Zhu, and M. Militzer: *Metall. Mater. Trans. A*, 2016, vol. 47A, pp. 3873–81.
16. R. Rosman and M.T. Rekveldt: *Phys. Rev. B*, 1991, vol. 43, p. 8437.
17. M.T. Rekveldt, N.H. van Dijk, S.V. Grigoriev, and W.G. Bouwman: *Rev. Sci. Instr.*, 2006, vol. 77, p. 073902.
18. S.G.E. te Velthuis, N.H. van Dijk, M.T. Rekveldt, J. Sietsma, and S. van der Zwaag: *J. Appl. Phys.*, 2001, vol. 89, pp. 1275–80.
19. H. Fang, S. van der Zwaag, and N.H. van Dijk: *Philos. Mag.*, 2018, vol. 98, pp. 1884–99.
20. S.G.E. te Velthuis, N.H. van Dijk, M.T. Rekveldt, J. Sietsma, and S. van der Zwaag: *Acta Mater.*, 2000, vol. 48, pp. 1105–14.
21. S.E. Offerman, L.J.G.W. van Wilderen, N.H. van Dijk, M.T. Rekveldt, J. Sietsma, and S. van der Zwaag: *Acta Mater.*, 2003, vol. 51, pp. 3927–38.
22. R. Rosman and M.T. Rekveldt: *J. Mag. Mag. Mater.*, 1991, vol. 95, pp. 319–40.
23. A.S. Arrott and B. Heinrich: *J. Appl. Phys.*, 1981, vol. 52, pp. 2113–15.
24. S. Sakarya, N.H. van Dijk, and E. Brück: *Phys. Rev. B*, 2005, vol. 71, p. 174417.
25. M. Kumar, R. Sasikumar, and P.K. Nair: *Acta Mater.*, 1998, vol. 46, pp. 6291–6303.
26. H. Chen and S. van der Zwaag: *Comput. Mater. Sci.*, 2010, vol. 49, pp. 801–13.
27. J.R. Bradley and H.I. Aaronson: *Metall. Mater. Trans. A*, 1981, vol. 12A, pp. 1729–41.
28. K. Oi, C. Lux, and G.R. Purdy: *Acta Mater.*, 2000, vol. 48, pp. 2147–55.
29. C. Capdevila, J. Cornide, K. Tanaka, K. Nakanishi, and E. Urones-Garrote: *Metall. Mater. Trans. A*, 2011, vol. 42A, pp. 3719–28.
30. A. Borgenstam, L. Höglund, J. Ågren, and A. Engström: *J. Phase Equil.*, 2000, vol. 21, pp. 269–80.
31. G.H. Zhang, R. Wei, M. Enomoto, and D.W. Suh: *Metall. Mater. Trans. A*, 2012, vol. 43A, pp. 833–42.
32. F. Danoix, X. Sauvage, D. Huin, L. Germain, and M. Gouné: *Scr. Mater.*, 2016, vol. 121, pp. 61–65.
33. J.M. Vitek, S.S. Babu., E. Kozeschnik: *Symposium on the Thermodynamics, Kinetics, Characterization and Modeling of austenite Formation and Decomposition, Materials Science and Technology Meeting*, 2003, pp. 139–48.
34. E. Cotrina, A. Iza-Mendia, B. López, and I. Gutiérrez: *Metall. Mater. Trans. A*, 2004, vol. 35A, pp. 93–102.
35. R. Bengochea, B. López, and I. Gutiérrez: *Metall. Mater. Trans. A*, 1998, vol. 29A, pp. 417–26.
36. H. Hänsel, L. Stratmann, H. Keller, and H.J. Grabke: *Acta Metall.*, 1985, vol. 33, pp. 659–65.
37. J. Sietsma and S. van der Zwaag: *Acta Mater.*, 2004, vol. 52, pp. 4143–52.
38. D.E. Coates: *Metall. Mater. Trans. B*, 1972, vol. 3B, pp. 1203–12.
39. M. Hillert: *Scripta Mater.*, 2002, vol. 46, pp. 447–53.
40. H. Oikawa: *Technol. Rep. Tohoku Univ.*, 1982, vol. 47, pp. 215–24.
41. H. Chen, M. Gounê, and S. van der Zwaag: *Comput. Mater. Sci.*, 2012, vol. 55, pp. 34–43.
42. J. Odqvist, M. Hillert, and J. Ågren: *Acta Mater.*, 2002, vol. 50, pp. 3213–27.
43. H.S. Zurob, D. Panahi, C.R. Hutchinson, Y. Brechet, and G.R. Purdy: *Metall. Mater. Trans. A*, 2013, vol. 44A, pp. 3456–71.
44. W.W. Sun, H.S. Zurob, and C.R. Hutchinson: *Acta Mater.*, 2017, vol. 139, pp. 62–74.
45. G.R. Purdy and Y.J.M. Brechet: *Acta Metall. Mater.*, 1995, vol. 43, pp. 3763–74.
46. M. Hillert: *Acta Mater.*, 1999, vol. 47, pp. 4481–4505.